Engineering 32 (2024) 127–137

Contents lists available at ScienceDirect

Engineering

journal homepage: www.elsevier.com/locate/eng

Research
Material Science and Engineering—Article

Electrical Resistivity Modification of Electrodeposited Mo and Mo–Co Nanowires for Interconnect Applications

Jun Hwan Moon [a,#], Taesoon Kim [a,#], Youngmin Lee [b,#], Seunghyun Kim [a], Yanghee Kim [c], Jae-Pyoung Ahn [c,d], Jungwoo Choi [b], Hyuck Mo Lee [b,*], Young Keun Kim [a,*]

[a] Department of Materials Science and Engineering, Korea University, Seoul 02841, Republic of Korea
[b] Department of Materials Science and Engineering, Korea Advanced Institute of Science and Engineering, Daejeon 34141, Republic of Korea
[c] Advanced Analysis Center, Korea Institute of Science and Technology, Seoul 02792, Republic of Korea
[d] Research Resources Division, Korea Institute of Science and Technology, Seoul 02792, Republic of Korea

ARTICLE INFO

Article history:
Received 1 January 2023
Revised 27 March 2023
Accepted 10 July 2023
Available online 27 October 2023

Keywords:
Molybdenum
Molybdenum–cobalt
Interconnect
Microstructure
Electrodeposition
Density functional theory

ABSTRACT

Achieving historically anticipated improvement in the performance of integrated circuits is challenging, due to the increasing cost and complexity of the required technologies with each new generation. To overcome this limitation, the exploration and development of novel interconnect materials and processes are highly desirable in the microelectronics field. Molybdenum (Mo) is attracting attention as an advanced interconnect material due to its small resistivity size effect and high cohesive energy; however, effective processing methods for such materials have not been widely investigated. Here, we investigate the electrochemical behavior of ions in the confined nanopores that affect the electrical properties and microstructures of nanoscale Mo and Mo–Co alloys prepared via template-assisted electrodeposition. Additives in an electrolyte allow the deposition of extremely pure metal materials, due to their interaction with metal ions and nanopores. In this study, boric acid and tetrabutylammonium bisulfate (TBA) were added to an acetate bath to inhibit the hydrogen evolution reaction. TBA accelerated the reduction of Mo at the surface by inducing surface conduction on the nanopores. Metallic Mo nanowires with a 130 nm diameter synthesized through high-aspect-ratio nanopore engineering exhibited a resistivity of (63.0 ± 17.9) μΩ·cm. We also evaluated the resistivities of Mo–Co alloy nanowires at various compositions toward replacing irreducible conventional barrier/liner layers. An intermetallic compound formed at a Mo composition of 28.6 at%, the resistivity of the Mo–Co nanowire was (58.0 ± 10.6) μΩ·cm, indicating its superior electrical and adhesive properties in comparison with those of conventional barriers such as TaN and TiN. Furthermore, density functional theory and non-equilibrium Green's function calculations confirmed that the vertical resistance of the via structure constructed from Mo-based materials was 21% lower than that of a conventional Cu/Ta/TaN structure.

1. Introduction

Copper (Cu) that has been metallized based on electrochemical damascene processes has survived as a primary interconnect material through several technology nodes. However, aggressive downscaling due to the high integration of integrated circuits (ICs) has continuously reduced the geometrical area of the back-end-of-line (BEOL). As a result, characteristics used to gauge device performance, such as electrical resistivity and reliability, have become progressively limited by the available interconnects. Two significant factors arise when the width of a metal conductor approaches several nanometers. First, when the local BEOL interconnect metal pitch becomes smaller than the electron mean free path (EMFP) of the interconnect material, electron scattering increases rapidly at the grain boundary and the surface or interface. This increase in electron scattering promotes resistive–capacitive delay and electromigration by intensifying the increase in linewidth resistance, generating heat. For example, the resistivity of a 10 nm-wide Cu interconnect line is approximately ten times higher than that of bulk Cu [1]. Second, the high diffusivity of Cu conductors into the

* Corresponding authors.
E-mail addresses: hmlee@kaist.ac.kr (H.M. Lee), ykim97@korea.ac.kr (Y.K. Kim).
# These authors contributed equally to this manuscript.

https://doi.org/10.1016/j.eng.2023.07.017

surrounding dielectric material causes short circuits in the interconnect, as well as chip failure. Although TaN has been adopted as a barrier due to its appropriate diffusion–prevention properties, Ta is inserted as a liner between the TaN and Cu, because the adhesion between TaN and Cu is not ideal. The TaN/Ta stack thins as the metal pitch decreases, but there is a limit to the minimum thickness (> 3 nm) required to carry out the role of each layer [2,3]. The irreducible thickness of the two indispensable layers significantly reduces the area occupied by the central conductor within the trench structure, and the relatively high resistivities constitute a significant bottleneck in the overall interconnect performance.

Thus, the demand for next-generation interconnect materials that can replace metallic Cu is growing. The figure of merit for the scaling of metal resistivity combines a low bulk resistivity (ρ_0) with a short EMFP (λ), $\rho_0 \times \lambda$. High cohesive energy is regarded as a proxy for resistance to electromigration and the need for diffusion barriers. Refractory metals that satisfy both requirements—such as cobalt (Co), ruthenium (Ru), rhodium (Rh), platinum (Pt), iridium (Ir), and molybdenum (Mo)—have been studied. Among several candidates, Co has recently been introduced as a material for the first two interconnect levels of commercial circuits with a titanium (Ti) liner/TiN barrier layer [4]. Although Co possesses a line resistance that is twice that of Cu in the nanoscale, it solves interconnection bottlenecks such as electromigration and high vertical via/contact resistance [4–6]. This tradeoff will be attractive to the industry if scaling continues. Ru is one of the most studied advanced materials; we have previously reported the electrical properties of electrodeposited Ru nanowires [7].

Introducing a new metallization material requires consideration of the surrounding environment. A new layer that can sustain liner and barrier scaling is needed, due to adhesion issues and to prevent the diffusion of the central conductor to the dielectric surroundings. Even if a conductor with excellent electromigration is adopted, it is necessary to find a suitable barrier/liner that interacts well with the central conductor for contact with the surrounding dielectric or for processing reasons. Considering these requirements, the single-alloy layer strategy is a good alternative. In previous reports, alloy materials such as RuCr, RuMo, RuW, CoW, and CoTi have been suggested to be effective for increasing the diffusion–prevention efficiency of the central conductor [8–12]. Furthermore, strong adhesion of the layer material to the central conductor can be realized if both systems possess similar crystal structures and lattices. Notably, intermetallic compounds formed from specific compositions, such as $CuAl_2$, NiAl, and $CuMg_2$, have been studied because they exhibit low resistivity and allow excellent adhesion to SiO_2 [13,14].

This study explores the potential of Mo-based metallization for the development of advanced interconnects. Mo-based interconnect materials are likely to significantly impact not only the performance and reliability of electronic devices but also the development of all-solid-state flexible energy-storage devices [15–17]. Mo exhibits low room-temperature resistivity (5.34 μΩ·cm), a shorter EMFP (11.2 nm) than that of Cu (39.9 nm) [18], and a high melting point (2623 °C). These three excellent properties make Mo a promising material for thin barriers or toward the achievement of barrierless integration [19,20]. However, in most previous studies investigating the potential of Mo, two-dimensional (2D) thin films were synthesized via vacuum deposition. For process compatibility with the additive damascene process, an electrodeposition-based process is needed to produce a confined conductor structure. To this end, we attempted to fabricate nanoscale Mo structures through template-assisted electrodeposition. We also aimed to reduce the thickness of the liner/barrier by alloying two elements, Co and Mo, to form a suitable liner/barrier layer for the Mo central conductor. Finally, we performed calculations based on density functional theory (DFT) and non-equilibrium Green's function (NEGF) to predict the change in via resistance depending on the candidate materials for an actual interconnect structure.

2. Experimental section

2.1. Synthesis of Mo and Mo–Co alloy nanowires

Mo-based nanowires were fabricated using track-etched polycarbonate membranes with a nominal average pore diameter of 100 nm (Whatman plc, UK) as templates. These membranes are capable of electrodepositing metallic nanowires with high aspect ratios. Before electrodepositing the Mo-based nanowires, a 300 nm silver (Ag) layer was deposited on one side of the template using an e-beam evaporator to form the cathode. The electrodeposited area of the porous template was 2 cm^2 (1 cm × 2 cm), which was prepared using an electrochemical cell. A Pt sheet was used as the counter electrode.

We obtained all reagents from Sigma-Aldrich (USA). To fabricate pure Mo nanowires, an electrolyte was prepared using potassium molybdate (K_2MoO_4, 0.01 mol·L^{-1}), ammonium acetate (CH_3CO_2-NH_4, 7.0 mol·L^{-1}), and potassium acetate (CH_3COOK, 1.0 mol·L^{-1}) in deionized water. Boric acid (H_3BO_3, 0.50 mol·L^{-1}) and tetrabutylammonium bisulfate (TBA; $(CH_3CH_2CH_2CH_2)_4N(HSO_4)$, 0.01 mol·$L^{-1}$) were added to the solution to inhibit the hydrogen evolution reaction (HER) during electrodeposition. A constant current of 10 mA·cm^{-2} was applied from a source meter to synthesize the pure Mo nanowires (Keithley 2611, Keithley, USA). To form the Mo–Co alloy nanowires, a citrate bath containing cobalt sulfate heptahydrate ($CoSO_4$·$7H_2O$, 0.20 mol·L^{-1}), potassium molybdate (K_2MoO_4), boric acid (H_3BO_3, 0.65 mol·L^{-1}), sodium citrate tribasic dihydrate ($C_6H_7Na_3O_8$), and citric acid ($C_6H_8O_7$, 0.04 mol·L^{-1}) was prepared. The composition of the Mo–Co alloy nanowires was controlled by varying the applied current density and additive concentration (Table 1). Inductively coupled plasma atomic emission spectroscopy (ICP-AES; Jobin Yvon Ultima 2, HORIBA Jobin Yvon, France) was employed to determine the Mo content under each synthesis condition. The other parameters and concentrations of the $CoSO_4$·$7H_2O$, H_3BO_3, and $C_6H_8O_7$ were constant for each electrodeposition bath.

After electrodeposition, the Ag layer was physically eliminated using tape. Then, the template was etched using dichloromethane (CH_2Cl_2) at 40 °C for 1 h. Finally, the nanowires were rinsed several times with chloroform ($CHCl_3$) and acetone (CH_3COCH_3) and dispersed in ethanol (CH_3CH_2OH). Post-deposition heat treatment was carried out at various temperatures for 1 h in a vacuum system (approximately 7 × 10^{-5} Torr (1 Torr = 133.322 Pa)).

2.2. Characterization

The morphologies of the Mo-based nanowires were investigated through high-resolution transmission electron microscopy (HR-TEM; JEM-2100F, JEOL Ltd., Japan). The effects of the additives and Mo content on the microstructures were determined by analyzing the selected-area electron diffraction (SAED) patterns acquired via HR-TEM. The crystal structures were analyzed through X-ray diffraction (XRD; D/MAX-2500 V/PC, Rigaku Corporation, Japan); the diffractometer was operated at 40 kV and 200 mA and was equipped with a Cu Kα radiation source. The average crystallite size was calculated using the Williamson–Hall method and HighScore Plus XRD analysis software (Malvern Panalytical, UK). A micro X-ray photoelectron spectrometer (XPS; AXIS-NOVA, Shmadzu, Japan) was employed to analyze the surface bonding of the Mo nanowires using Al Kα radiation (1486.6 eV). The pass energy for narrow scans was 0.05 eV. After subtracting

Table 1
Mo content of the Mo–Co alloy nanowires under various experimental conditions.

K_2MoO_4 ($mol·L^{-1}$)	$C_6H_7Na_3O_8$ ($mol·L^{-1}$)	Current density ($mA·cm^{-2}$)	Mo content (at%)
0.25	0.25	2.50	5.6
0.25	0.50	2.50	13.2
0.25	0.30	10.00	28.6
0.50	0.50	10.00	43.6

the background, a combined Gaussian–Lorentzian function was used to fit the photoemission results. The effect of additives on Mo synthesis was investigated using a three-electrode system. Pt foil and Ag/AgCl (3 $mol·L^{-1}$ NaCl) were used as the counter and reference electrodes, respectively. The electrode potential was calibrated to the scale of the reversible hydrogen electrode (RHE): E (vs RHE) = E (vs Ag/AgCl) + 0.05916pH + 0.210, the unit of E is voltage (V).

To accurately measure the electrical properties of the nanowires, a four-point probe method was adopted in order to avoid measurement errors caused by contact resistance. Before measurement, the Mo-based nanowires were dispersed on a silicon substrate with a 300 nm layer of SiO_2 and vacuum-packed to minimize oxidation caused by air exposure. The upper SiO_2 layer prevents current leakage that may occur during the measurement process. Four nanomanipulators (MM3A EM, Klindiek, Germany) attached to a focused ion beam (FIB; Quanta 3D, FEI, USA) were used to measure the nanosized specimens. A pressure of 2.3×10^{-5} Torr was maintained in the FIB chamber during the measurements. One dispersed nanowire was selected and fixed by depositing Pt using focused electron beam deposition. Before every measurement, the tungsten (W) tip was etched at 30 kV and 0.5 nA for 5 s using a Ga^+ ion beam generated by the FIB instrument to remove the native oxide. Subsequently, the four W tips of the nanomanipulator were placed in direct contact with the nanowire to measure the electrical properties.

2.3. Computational details

Computer simulations of the interfacial binding energies were performed using DFT, as implemented in the Vienna *Ab-Initio* Simulation Package (VASP; University of Vienna, Austria) [21,22]. The generalized gradient approximation (GGA) of the Perdew–Burke–Ernzerhof (PBE) exchange-correlational functional was used [23]. The convergence criteria for the electronic structure and mean force were set to 10^{-4} eV and 0.01 $eV·Å^{-1}$, respectively. A kinetic energy cutoff of 500 eV and a $3 \times 3 \times 1$ Monkhorst–Pack k-point grid were selected for all the calculations. Supercells containing barrier/substrate interfaces were modeled using $Co_3Mo(201)$ and TaN(0001) as the barrier materials and Mo(110) and $SiO_2(001)$ as the substrates. Mo(110) and $Co_3Mo(201)$ exhibited high-intensity XRD patterns, while other planes had the most closely packed surfaces with the lowest surface energy. Half the substrate layers in the bulk position were fixed, and a vacuum layer thickness of at least 2 nm was adopted.

The interfacial binding energy per cross-sectional area (E_{int}) was calculated according to Eq. (1):

$$E_{int} = \frac{(E_{lin/sub} - E_{sub} - E_{lin})}{A} \quad (1)$$

where $E_{lin/sub}$ is the total energy of the system, E_{sub} is the energy of the isolated substrate, and E_{lin} is the energy of the isolated liner. The energy terms were normalized using the cross-sectional area (A).

NEGF transport calculations using the Synopsys QuantumATK software (Synopsys, USA) package were used to calculate the electrical properties [24]. The GGA was used as the exchange–correlation function. Fritz–Haber Institute (FHI) pseudopotentials, a double-zeta polarized basis set, and a cutoff mesh energy of 100 Hartree (1 Hartree = 2625.5 $kJ·mol^{-1}$) were applied [23,25]. All geometries were relaxed until the force acting on each atom was less than 0.05 $eV·Å^{-1}$. The k-point density for the transport calculations was $4 \times 4 \times 150$. A two-probe device configuration with a central scattering region including the liner materials was constructed, and electron transmission at the Fermi energy was calculated for the relaxed structures. The conductance, G, was calculated from the transmission at the Fermi energy and normalized by the cross-sectional area to obtain the specific resistivity.

3. Results and discussion

3.1. Electrodeposition of Mo nanowires on high-aspect-ratio nanopores

We fabricated Mo nanowires with different additives in a single bath to investigate the effect of their purity on their electrical resistivity. Mo electrodeposition involves a competing HER due to the high negative reduction potential of molybdate ions. In addition, the continuous consumption of protons at the cathode increases the local pH, contaminating pure Mo with basic salts or hydroxides. Therefore, numerous buffering agents have been used to deposit impurity-free Mo by reducing the pH around the electrode. For example, previous studies reported that a combination of acetate and ammonia was an excellent additive for depositing pure Mo [26,27]. We utilized a high-concentration acetate bath containing 7.0 $mol·L^{-1}$ ammonium acetate and 1.0 $mol·L^{-1}$ potassium acetate to inhibit the HER while maintaining the pH of the solution. To investigate the correlation between the electrodeposition of pure Mo nanowires and the HER, we added boric acid and TBA as HER inhibitory additives to the aqueous electrolytes. Mo nanowires synthesized in the acetate bath were labeled Mo(A), those synthesized in the presence of acetate and boric acid were labeled Mo(AB), and those synthesized in the presence of acetate, boric acid, and TBA were labeled Mo(ABT).

We evaluated the electrical properties accurately, relying on an FIB instrument equipped with four W nanomanipulators, as shown in Fig. 1(a). The average measured diameter of the nanowires was approximately 130 nm. We obtained the resistance of a single nanowire, R_{ohm}, from the ΔV–current (I) graph, as shown in Fig. 1(b). We then calculated the electrical resistivity of a single nanowire, ρ_{NW}, using Eq. (2):

$$\rho_{NW} = \pi r^2 \frac{R_{ohm}}{\Delta L} \quad (2)$$

where r and ΔL represent the measured radius of a single nanowire and the distance between the two middle probe tips, respectively. The resistivity of the synthesized Mo nanowires varied significantly depending on the type of additive, as shown in Fig. 1(c). The resistivity of Mo(A) was (1362.8 ± 542.3) μΩ·cm, indicating dominance by MoO_2 [28,29], while that of Mo(ABT) was (410.1 ± 87.3) μΩ·cm, which was reduced by approximately 70% in relation to the resistivity of Mo(A). Surprisingly, the resistivity of Mo(AB) was (63.0 ± 17.9) μΩ·cm, the lowest value measured, indicating mainly pure Mo [28]. In the classical transport model, the electrical resistivity of a nanomaterial is the sum of the contributions of the surface scattering [30] and grain-boundary scattering [31] to the bulk resistivity. Due to the contribution of surface scattering, the resistivities of one-dimensional nanowires are generally higher than those of 2D thin films. Above all, the concentration of impurities increases the resistivity.

Furthermore, we conducted microstructural analyses to elucidate the effect of the electrolyte on the electrical resistivity. According to the TEM and XRD data in Fig. 2, Mo nanowires

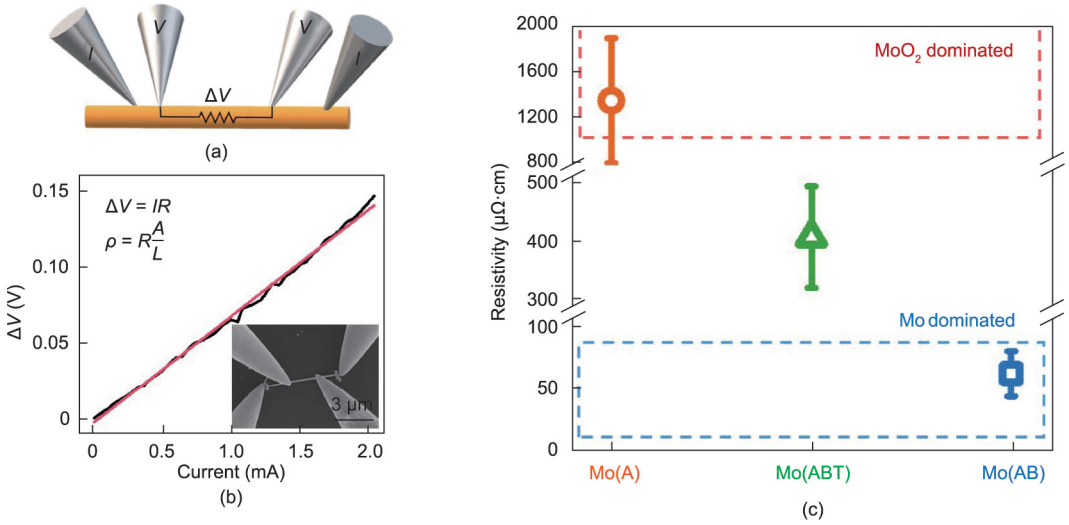

Fig. 1. *In situ* four-point probe electrical measurement of a single nanowire and resistivity results according to the additive type. (a) Schematic of the *I*–Δ*V* measurements using four W tips. (b) Electrical resistance of a single Mo nanowire with a diameter of 130 nm; the fitted line indicates an ohmic contact (inset: scanning electron microscopy image of the real-time measurement of a single nanowire). (c) Resistivity changes of the synthesized single Mo nanowires with different additive types. Regions of reference values for different Mo phases are outlined by dashed-line rectangles [20,28,29].

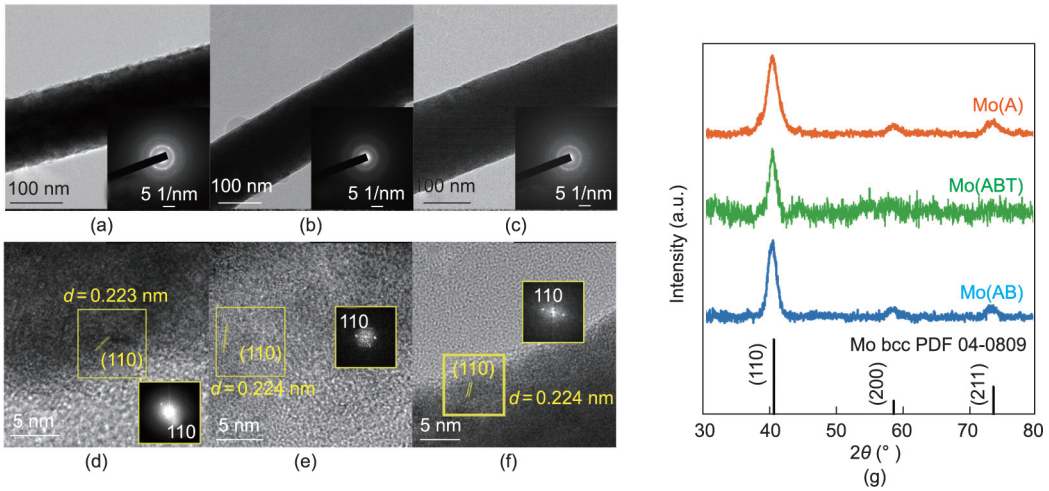

Fig. 2. Morphologies and microstructures of the synthesized Mo nanowires. (a–c) TEM images of the (a) Mo(A), (b) Mo(ABT), and (c) Mo(AB) nanowires. The SAED patterns in the inset show a weak crystalline or nanocrystalline state under three conditions. (d–f) HR-TEM images at the termination of the (d) Mo(A), (e) Mo(ABT), and (f) Mo(AB) nanowires. The measured interlayer distance and corresponding fast-Fourier-transform pattern confirm the presence of Mo(110). (g) XRD patterns of the Mo(A) (orange), Mo(ABT) (green), and Mo(AB) (blue) nanowires. The reference peak for bcc Mo (Powder Diffraction File (PDF) No. 04–0809) is displayed below the XRD patterns.

prepared under each electrolyte condition possessed similar body-centered cubic (bcc) crystal structures, regardless of the electrolyte type. The SAED patterns measured with an objective aperture with a diameter of 180 nm indicated that most of the Mo nanowires were polycrystalline (Figs. 2(a)–(c)). The HR-TEM images in Figs. 2(d)–(f) reveal interplanar distances of 0.223, 0.224, and 0.224 nm, respectively, which are almost identical to the interplanar distance of 0.223 nm in the (110) plane of Mo. These results are consistent with the dominant XRD pattern observed under all electrolyte conditions—that is, the pattern corresponding to the Mo(110) plane (Fig. 2(g)). Because the Mo nanowires have an anisotropic shape and a low degree of texture, we calculated the average crystallite size using the Williamson–Hall method, presented in Eq. (3):

$$\beta_{hkl} = \beta_{size} + \beta_{strain} = \frac{K\Lambda}{D\cos\theta} + 4\varepsilon\tan\theta \quad (3)$$

where β_{hkl} is the full width at half maximum (FWHM) intensity, β_{size} is the FWHM contribution by crystallite size, β_{strain} is the FWHM contribution by strain, D is the mean crystallite size, θ is the Bragg angle, K is a dimensionless shape factor of about 0.9, Λ is the X-ray wavelength, and ε is the strain. Diffraction peaks are usually the convolution of a Lorentzian profile due to the presence of nanocrystallites and a Gaussian profile due to the lattice microstrain. Therefore, we analyzed the contributions of these two components using the pseudo-Voigt function after correcting the instrumental broadening. We derived the crystallite size and microstrain values from the *y*-intercept and slope of the linearly fitted graph, respectively (Fig. S1 in Appendix A). The derived crystallite sizes of the Mo(A), Mo(ABT), and Mo(AB) nanowires were 2.63, 3.89, and 5.37 nm, respectively. The resistivity decreased with increasing crystallite size, as shown in Fig. 1(c).

Although the crystallite size contributes to the resistivity, we cannot completely exclude the contribution of impurities. When Mo is electrodeposited in a confined nanopore, three main factors need to be considered (Fig. 3(a)): ① The HER competes with electron transfer to the Mo precursors, and hydrogen trapped in

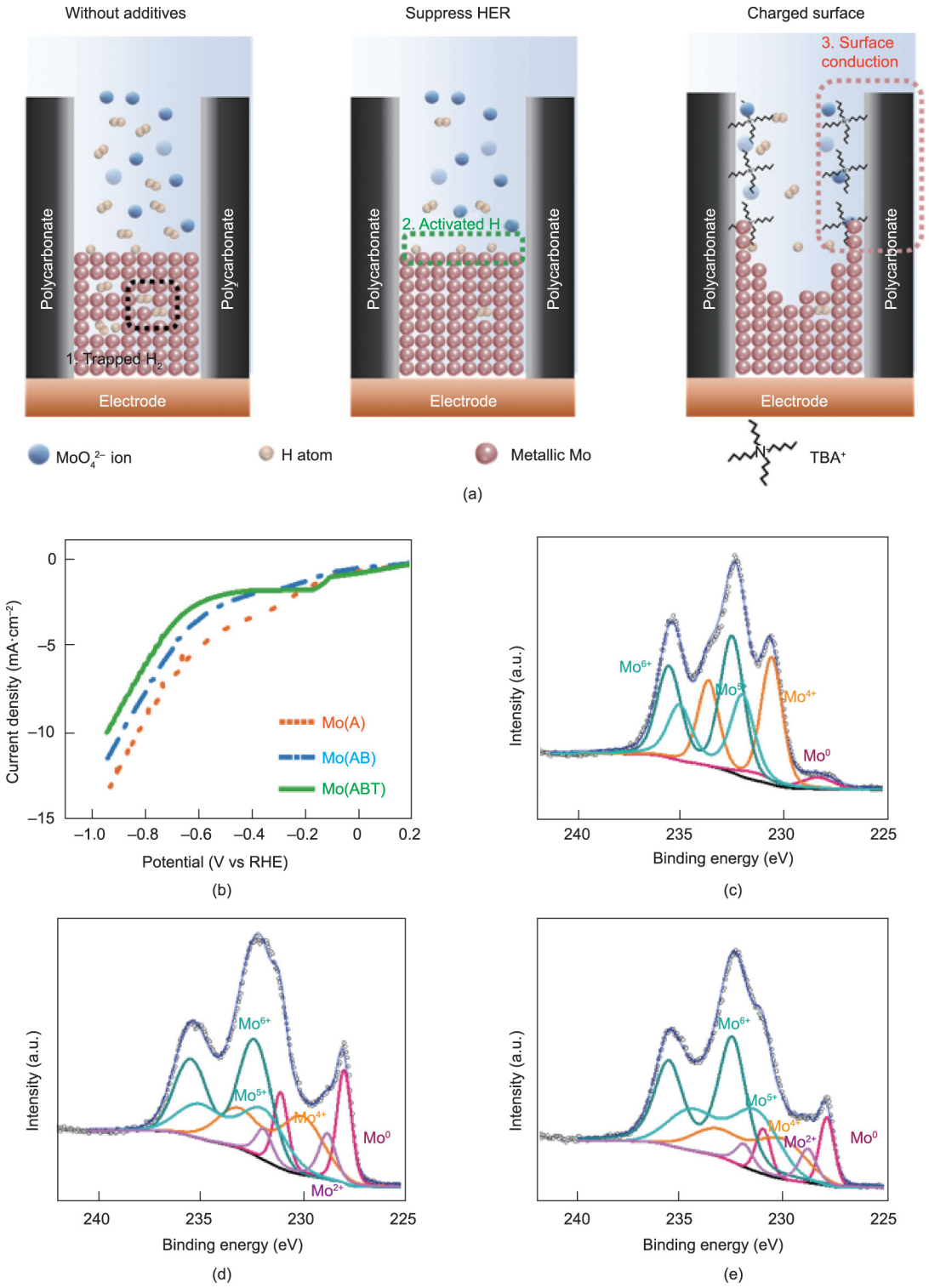

Fig. 3. Different electrodeposition mechanisms of the nanowires according to the additive type. (a) Schematic of the formation of Mo nanowires in high-aspect-ratio confined nanopores. Three main factors influence the electrodeposition of Mo and are controllable by adjusting the additive type. (b) HER polarization curves for Mo(A) (orange), Mo(AB) (blue), and Mo(ABT) (green) baths. We carried out measurements in the same electrochemical cell used for synthesis. (c–e) High-resolution Mo X-ray photoelectron spectra of the (c) Mo(A), (d) Mo(ABT), and (e) Mo(AB) nanowires.

the Mo crystals causes the amorphization of the Mo nanowires. ② Activated hydrogen is adsorbed onto multivalent Mo oxide to aid further reduction. ③ Surface conduction due to the electric double layer (EDL) formed along the inner wall of the pores plays an important role. The direct reduction of MoO_4^{2-} (used as a precursor in this study) to Mo involves six electron transfers.

$$MoO_4^{2-}(aq) + 4H_2O(l) + 6e^- \rightarrow Mo(s) + 8OH^-(aq) \quad (E^0 = -0.913\ V) \tag{4}$$

In contrast, the following two equations occur predominantly at the cathode, due to the lower electron transfer and higher potential:

$$MoO_4^{2-}(aq) + 2H_2O(l) + 2e^- \rightarrow MoO_2(s) + 4OH^-(aq) \quad (E^0 = -0.780\ V) \tag{5}$$

$$2H_2O(l) + 2e^- \rightarrow H_2(g) + 2OH^-(aq)\ (E^0 = -0.828\ V) \tag{6}$$

Reactions (5) and (6) are favorable because they require less electrochemical energy transfer than reaction (4). Therefore, a highly concentrated acetate bath was adopted, in which boric acid and TBA inhibited the HER.

Fig. 3(b) compares the typical HER polarization curves of the Mo(A), Mo(AB), and Mo(ABT) baths. Voltammetry experiments performed in the electrochemical cell revealed that the HER was most active in the Mo(A) bath and least active in the Mo(ABT) bath. In agreement with the HER polarization curves, the X-ray photoelectron (XP) spectra provided in Figs. 3(c)–(e) for each nanowire show the degree of Mo reduction at the surface (Fig. S2 in Appendix A). The surface of the Mo(A) nanowires subjected only to the acetate bath contained several forms of Mo oxide, suggesting that high concentrations of acetate additives alone have limited HER inhibition and that additional processing is required to electrodeposit metallic Mo.

In contrast, the XP spectra of Mo(ABT) and Mo(AB) with additives revealed higher amounts of the pure Mo metal than the XP spectrum of Mo(A). A shoulder peak with a low valence state appeared near the Mo^0 peak. According to the voltammetry curve and XPS results, the Mo reduction reaction was most active in the Mo(ABT) nanowires, which are predicted to induce the lowest resistivity. However, the measured resistivity and crystallinity of the Mo(AB) nanowires were high. We attribute this phenomenon to the surface conduction acting as the dominant mechanism on the inner wall of the nanopore, causing the flow of an overlimiting current (OLC) that reduces Mo in the confined nanopore. When a solid is immersed in an ionic solution, an EDL is formed between the solid and solution interface under the influence of the surface charge generated upon polarization [32,33]. A lower precursor concentration increases the EDL thickness; the metallic ions to be reduced must pass through the thick EDL along the high-aspect-ratio pores. As the electric field intensity increases in such a severe environment, a depletion region is created in front of the cathode when ion transfer reaches a critical point, and a plateau arises with a flowing current. Applying an OLC beyond this flat region causes a high current to flow along the nanopore surface. The interaction of specific ions with the inner walls of the nanopores reinforced this phenomenon. In particular, the positively charged nanopores around the cathode increased the surface charge to reduce the metal ions along the inner walls of the nanopores, enabling nanotube synthesis [33,34].

To summarize, the TBA cation was used as an additive to inhibit the HER and increase the surface conduction in our experiment. As shown in Fig. 3(b), the Mo(ABT) polarization curve displays a section where the current density is constant, unlike that observed in the other baths. Furthermore, the results of the surface analysis at a depth of about 5 nm via XPS indicated that TBA enhanced the surface charge, helping to reduce the metal. However, the Mo of Mo(ABT) was not relatively reduced in the pore center due to the increased surface charge, showing lower crystallinity and higher resistivity than those of Mo(AB) (Fig. 1(c)).

3.2. Effect of Mo atom intrusion on Mo–Co alloy nanowires

The introduction of new central conductors and the inability to overcome the limitations of the liners and barriers used in current processes require an alternative material approach. This could include considering a crystal structure with low resistivity at the nanoscale, preventing diffusion, and increasing adhesion with the central conductor. To explore alternative liner/barrier materials, we investigated Mo and Co alloys, which are emerging as advanced interconnect materials. We fabricated Mo–Co alloy nanowires in a bath containing citrate ions (Fig. S3 in Appendix A). The citrate ions combined with Co^{2+} and MoO_4^{2-} ions to form adsorption intermediates, inducing the final reduction of the Mo–Co alloy [35,36]. Fig. 4 displays the dependence of the Mo composition on the resistivity of the Mo–Co alloy nanowires. The green and blue lines show the resistivities of the Mo_xCo_{1-x} (0.05 at% < x < 0.44 at%) nanowires in the as-deposited state and after heat treatment at 600 °C for 1 h, respectively. The electrical resistivity of the as-deposited nanowires depends on the Mo content in two sections. The incorporation of Mo into the Co lattice gradually increases the resistivity from (45.1 ± 8.3) to (105.5 ± 5.6) μΩ·cm as the Mo content increases from 5.6 at% to 28.6 at%.

By further increasing the Mo content to 43.6 at%, the resistivity drastically increased to (269.2 ± 10.9) μΩ·cm. The overall resistivity variation in the as-deposited sample followed Nordheim's rule, with a parabolic function [37]. Considering that the typical resistivity of a TaN thin film with a thickness similar to the diameter of the fabricated nanowire is 250–400 μΩ·cm [38,39], the Mo–Co alloy is advantageous in terms of electrical properties below a specific composition. We measured the electrical resistivity after annealing at 600 °C for 1 h to remove internal defects and create an aligned phase. While the as-deposited Mo–Co alloy nanowire exhibited the electrical properties of a general solid solution, the electrical resistivity trend exhibited peculiar behavior near 28.6 at% Mo after heat treatment (blue line). The resistivity of the alloy nanowires after heat treatment was (62.2 ± 0.7) μΩ·cm at 13.2 at% Mo and (105.5 ± 31.7) μΩ·cm at 43.6 at% Mo. In comparison, the resistivity of the alloy nanowire incorporating 28.6 at% Mo was (58.0 ± 10.6) μΩ·cm, which was lower than that of the nanowires with other Mo concentrations.

We obtained powder XRD patterns of the as-deposited nanowires (Fig. 5(a)) to elucidate the effect of microstructural changes in the Mo–Co alloy nanowires as a function of Mo content. The XRD patterns indicated that hexagonal closed-packed (hcp) Co is the dominant species and confirmed the presence of trace amounts of Mo atoms. A gradual transformation to the amorphous state was observed as the Mo solute was accommodated into the Co matrix.

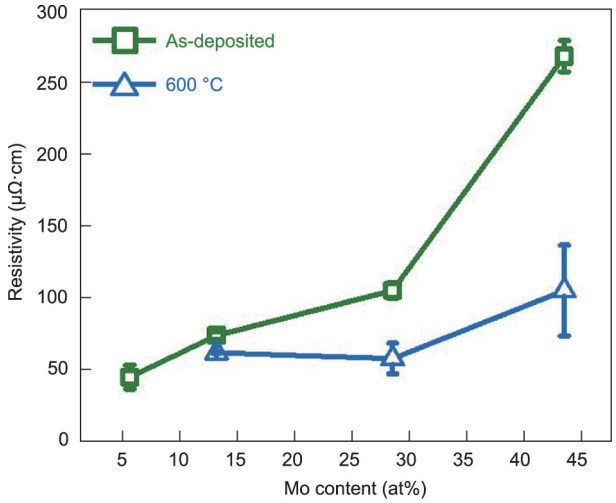

Fig. 4. Experimental resistivity values of the Mo_xCo_{1-x} (0.05 < x < 0.44) alloy nanowires with a diameter of 130 nm. Note that the resistivity of TaN with a thickness similar to the synthesized nanowire diameter is > 250 μΩ·cm.

In detail, the XRD patterns of the alloys containing up to 13.2 at% Mo featured an hcp Co(100) peak; however, this peak trails off for alloys with Mo contents of > 28.6 at%. Moreover, Fig. 5(b) shows the magnified XRD peaks in the 2θ range of 45°–49°, revealing that the peak position shifts to the left with increasing Mo content. This peak broadening indicates a further decrease in the crystallite size with increasing Mo content. As Mo atoms, which have a relatively large radius, penetrate the Co matrix, wherein the Co atoms have a smaller radius, the average distance (d_{avg}) between the two adjacent atoms is described by the following equation [40]:

$$d_{avg} = 2[r_{Co} + (r_{Mo} - r_{Co}) \cdot \chi_{Mo}] \quad (7)$$

where r_{Co} and r_{Mo} are the atomic radii of Co and Mo, respectively, and χ_{Mo} is the atomic fraction of Mo in the alloy. In substitutional alloy systems, the interplanar distance affects the position of the peaks according to the Bragg equation:

$$d_{avg} = \frac{\xi}{2\sin\theta} \quad (8)$$

where ξ is the Cu Kα wavelength and 2θ is the peak position.

Fig. 5(c) reveals the dependence of the crystallite size on the amount of Mo, calculated according to the Williamson–Hall method. The average crystallite size of the as-deposited 5.6 at% Mo nanowires is 15.8 nm, which decreases with increasing Mo content. According to the XRD patterns and calculated crystallite size, the as-synthesized Mo–Co alloy nanowires are considered to be solid solutions, in which Mo penetrates the hcp Co matrix at up to 13.2 at%. When the Mo content is increased to 28.6 at%, the crystals of hcp Co do not easily form and take on a polycrystalline form with an average crystallite size of 3.2 nm. Eventually, an amorphous phase appears when the crystallite size is significantly decreased to < 2.6 nm, as evidenced by the appearance of broad peaks in the XRD pattern of Co_3Mo. The green line representing the resistivity in Fig. 4 and the crystallite size in Fig. 5(c) exhibit an inverted trend. The decrease in the crystallite size and the degradation of the crystallinity due to Mo atom incorporation promote electron scattering inside the nanowire, contributing to the increase in resistivity. Notably, the significant difference in resistivity values between the two compositions (28.6 at% and 43.6 at%) with similar average crystallite sizes indicates that the solid-solution effect is the major contributor, along with nanocrystallization.

To precisely determine the microstructure and components of the Mo–Co alloy nanowires, we investigated the effect of the heat-treatment temperatures on the microstructures, as illustrated in Fig. 6. Because heat treatment induces recrystallization and thermodynamically stabilizes the phase transition [41], the XRD patterns of the nanowire annealed at 600 °C for 1 h contain sharp peaks for all compositions, as shown in Fig. 6(a). In the equilibrium phase diagrams of Mo and Co [42], the electrodeposited Mo–Co alloy nanowires appeared to undergo thermodynamic phase separation according to their composition. At low Mo content, the hcp Co matrix undergoes a phase transition to face-centered cubic (fcc) Co, and a small amount of Co combines with Mo to form the hcp Co_3Mo phase. As the Mo content increases, the fcc Co peak intensity gradually decreases, and most of the Mo atoms near Co_3Mo (28.6 at% Mo) are in the Co_3Mo phase. As shown in Figs. 6(b) and (c), the peaks in the XRD patterns are in the 2θ range of 40°–48° for the nanowires comprising 13.2 at% and 28.6 at% Mo; these patterns clearly indicate the disappearance of the fcc Co(111) peak with the increase in the Mo content. Subsequently, when the Mo content increases to 43.6 at%, it is confirmed that the MoO_2 phase co-exists with the Co_3Mo phase. Corresponding to previous reports [43,44], if the Mo content of the solution increases during

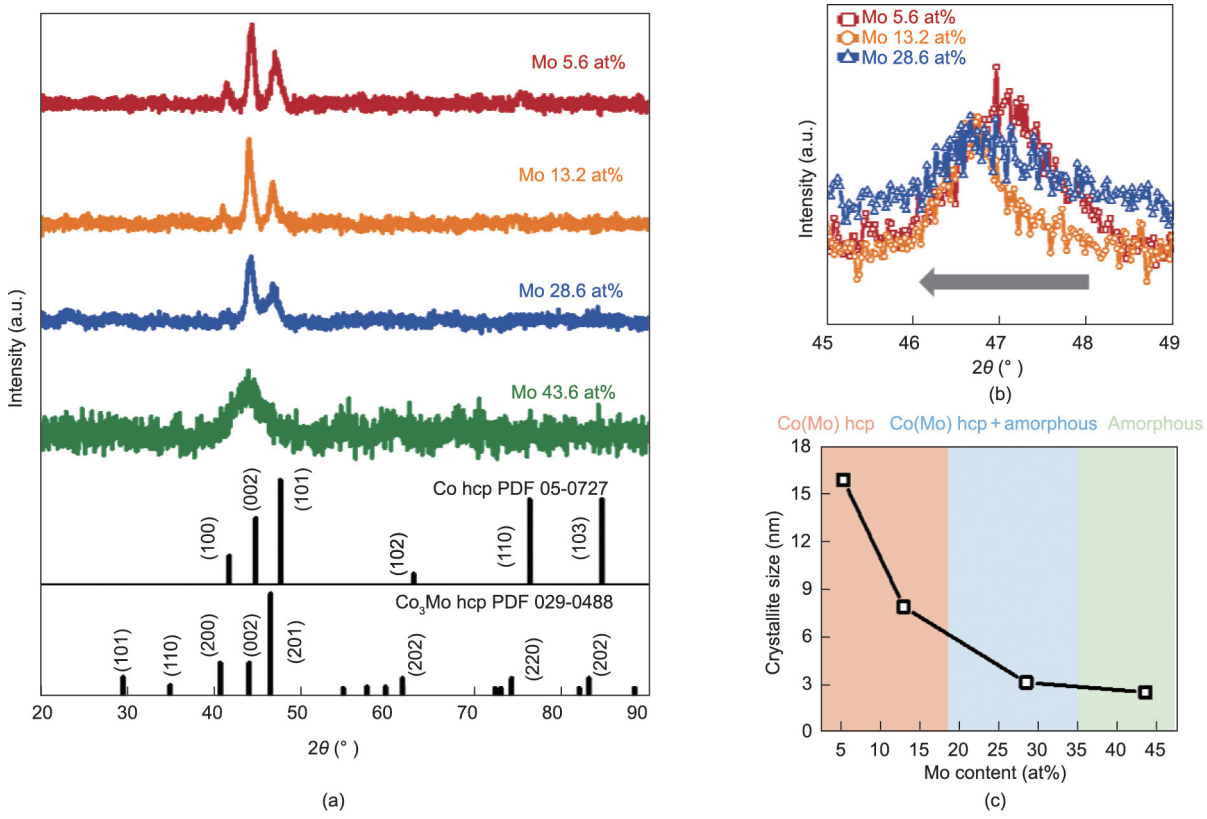

Fig. 5. Effect of the Mo content of the as-deposited Mo_xCo_{1-x} ($0.05 < x < 0.44$) alloy nanowires on microstructure and crystallite size. (a) XRD patterns of the Mo–Co alloy nanowires with varying Mo contents. The line patterns show the phases of hexagonal closed-packed (hcp) Co (PDF No. 05–0727) and hcp Co_3Mo (PDF No. 029–0488). (b) Magnified XRD patterns (2θ = 45°–49°). (c) Calculated crystallite size distribution as a function of the Mo content of the Mo–Co alloy nanowires.

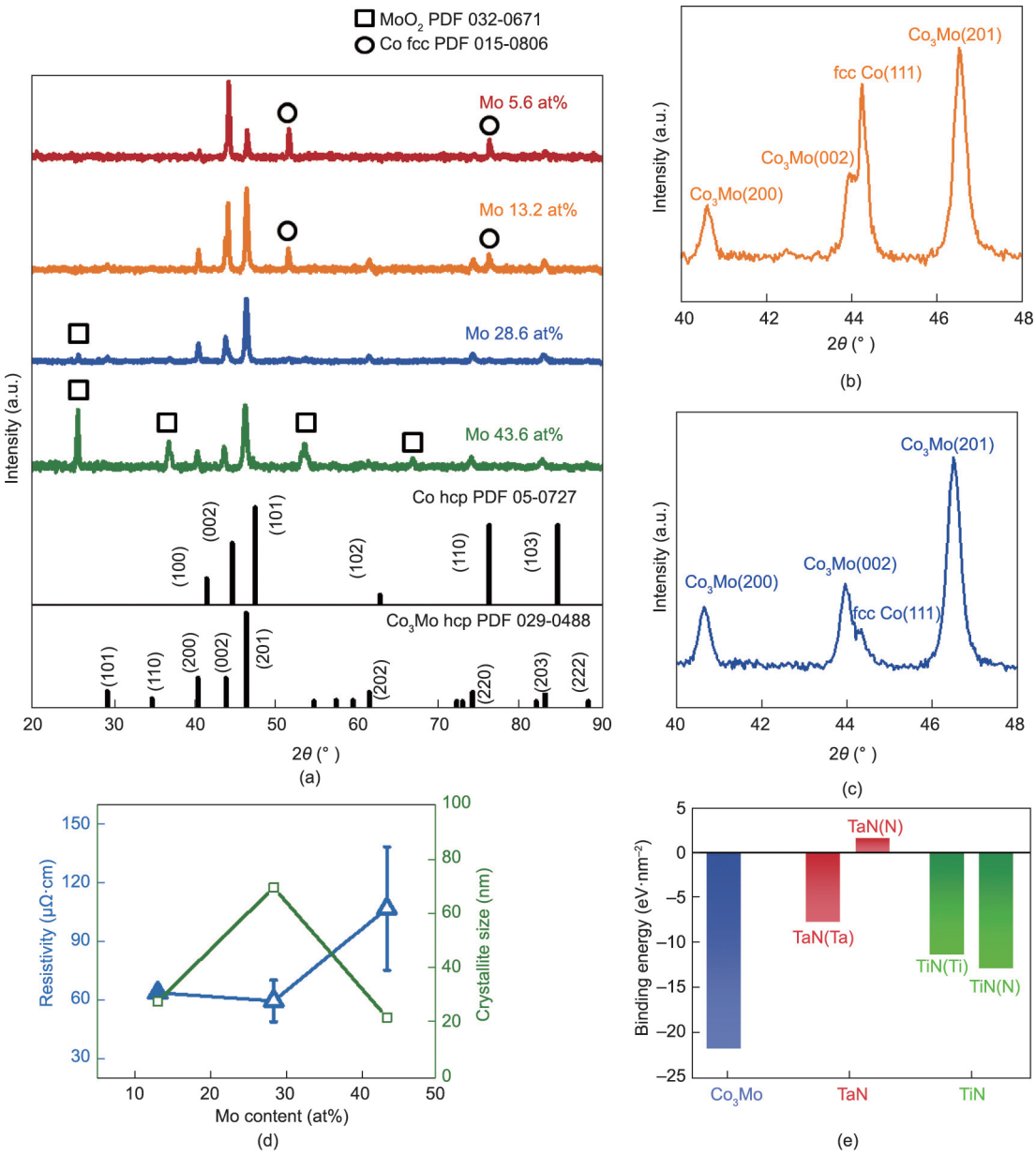

Fig. 6. Formation and characterization of the Co_3Mo intermetallic compound. (a) XRD patterns of the Mo–Co alloy nanowires after heat treatment at 600 °C for 1 h. For ease of comparison, we show the XRD pattern for the hcp Co phase, but most of the Co underwent a transformation to the face-centered cubic (fcc) phase. (b, c) Magnified XRD patterns of (b) 13.2 at% and (c) 28.6 at% Mo nanowires. (d) Changes in the electrical resistivity according to the Mo composition after heat treatment. (e) Calculated Mo/barrier adhesion energy values for Co_3Mo, TaN, and TiN barriers. The barrier (termination element) indicates the terminal element of the barrier material that comes into contact with Mo at the interface, where large negative values indicate stronger adhesion with the Mo conductor.

electrodeposition, the citrate ion does not generate sufficient intermediates, impeding the reduction of metallic Mo. Therefore, we presume that Mo oxides coexist in the 43.6 at% Mo nanowires, even in the as-deposited state before heat treatment.

We conducted additional investigations on the 28.6 at% Mo alloy nanowires to determine the applicability of the Co_3Mo intermetallic compound as a liner/barrier in the advanced metallization process. Within the thermal budget of the BEOL (< 400 °C), the Co_3Mo intermetallic compound exists in the form of nanocrystallites, similar to the as-deposited state (Fig. S4 in Appendix A). The crystallite size increased slightly from 3.2 to 5.4 nm after heat treatment at 400 °C. When the heat-treatment temperature was increased to 600 °C, the crystallite size of the Co_3Mo intermetallic compound with an ordered phase increased sharply to 68.7 nm in relation to the crystallite sizes of 27.0 nm (13.2 at% Mo) and 21.1 nm (43.6 at% Mo) for the other compositions, as illustrated in Fig. 6(d). Consequently, the electrical resistivity of the alloy nanowires after heat treatment was inversely proportional to the crystallite size.

In addition to the electrical properties, adhesion is a crucial feature of interconnects. We calculated the bonding energy between the Mo(110) and $Co_3Mo(201)$ surfaces using first-principles calculations based on the XRD results of this study. For comparison, we calculated the binding energies between the Mo(110) and state-of-the-art barrier (i.e., TaN(0001) and TiN(100)) surfaces. Because adhesion depends on the termination of the material during

interface formation, we calculated the conventional barrier material for the interface formed with Mo by dividing the metal and nitrogen. The calculated binding energies are plotted in Fig. 6(e) and tabulated in Table S1 (Appendix A). The contact at the interface is favorable when the adhesion value is negative and unfavorable when the value is positive, such as the N of TaN, which represents termination. Hence, Co_3Mo has better contact with Mo conductors and electrical properties that are superior to those of conventional barriers.

3.3. DFT–NEGF simulations of Mo-based materials in the conventional structure

The interconnect consists of a multilayered structure that transfers the external driving current to the desired transistor. A series of vertical connections called via structures connect several horizontal layers. The electrical resistance bottleneck of the interconnect structure worsens in the via structure locations where the liner and barrier resistances are involved in the driving current. We used two-terminal NEGF transfer calculations to predict the decrease in the electrical resistance of via structures in actual wiring structures (Fig. 7). We considered two interface structures constructed with two semi-infinite Mo and Cu electrodes. To construct a supercell with a countable number of atoms while including the XRD results of the nanowires synthesized by electrodeposition, we considered electron transport along bcc Mo(110) and hcp Co_3Mo(201). We assumed that Cu, Ta, and TaN had fcc, bcc, and hcp crystal structures, respectively. The fcc Cu(111) orientation was adopted on the basis of experimental observations in damascene interconnects [45,46]. We set the total thickness of the liner/barrier to 3 nm, which is the minimum thickness required for each layer to achieve the intended purpose in conventional Cu damascene, and assumed that the thickness of the liner and barrier were identical. The two-terminal NEGF calculation expresses the electron conductance as a linear response based on the Landauer formula at low bias:

$$G = \frac{e^2}{h}\sum_i T_i(E_F) = \frac{1}{R} \tag{9}$$

where G is the conductance, e is the charge of an electron, h is Plank's constant, and $T_i(E_F)$ is the transmission for the ith electronic channel at the Fermi energy. Finally, we normalized the R value obtained from the derived G value to the cross-sectional area of the supercell. This approach is similar to that used in previous studies [47,48].

Figs. 7(b)–(e) present the cross-sectional images of atomic-scale interface configuration representations. Fig. 7(b) shows the reference Cu/α-Ta(1.5 nm)/TaN(1.5 nm)/Cu structure, and Fig. 7(c) depicts the Mo/α-Ta(1.5 nm)/TaN(1.5 nm)/Mo structure. In these structures, Mo was applied as the central conductor to the conventional liner/barrier bilayer. The liner/barrier bilayer was replaced with a single Co_3Mo intermetallic compound to assume the via structure of Mo-based materials. Figs. 7(d) and (e) show the Mo/Co_3Mo(3.0 nm)/Mo and Mo/Co_3Mo(1.5 nm)/Mo structures, respectively. For comparison, we listed the calculated $T(E_F)$, cross-sectional area, and area-normalized vertical resistance (γ) of each supercell in Table 2. The Mo electrode applied to the conventional liner/barrier bilayer shows an approximately 28.3% increase in vertical resistance in relation to the reference structure. This result suggests that introducing a new Mo conductor requires the exploration of another new material, as shown in the adhesion result in Fig. 6(e). In contrast, when we replaced the conventional bilayer with a 3 nm-thick Co_3Mo layer, the vertical resistance was reduced by 21.5% in relation to that of the reference structure. Moreover, when we reduced the thickness of the Co_3Mo layer to 1.5 nm, the vertical resistance decreased to 3.57×10^{-11} Ω·cm^2, which is 69.1% lower than that of the conventional structure.

Table 2
Calculated transmissions at the Fermi energy, cross-sectional area, and area-normalized vertical resistance (γ) for each interface structure.

Structure	$T(E_F)$	Area (Å^2)	γ ($\times 10^{-12}$ Ω · cm^2)
Cu/α-Ta(1.5 nm)/TaN(1.5 nm)/Cu	0.51	45.95	115.50
Mo/α-Ta(1.5 nm)/TaN(1.5 nm)/Mo	0.42	48.23	148.20
Mo/Co_3Mo(3 nm)/Mo	0.78	55.04	90.63
Mo/Co_3Mo(1.5 nm)/Mo	1.99	55.04	35.71

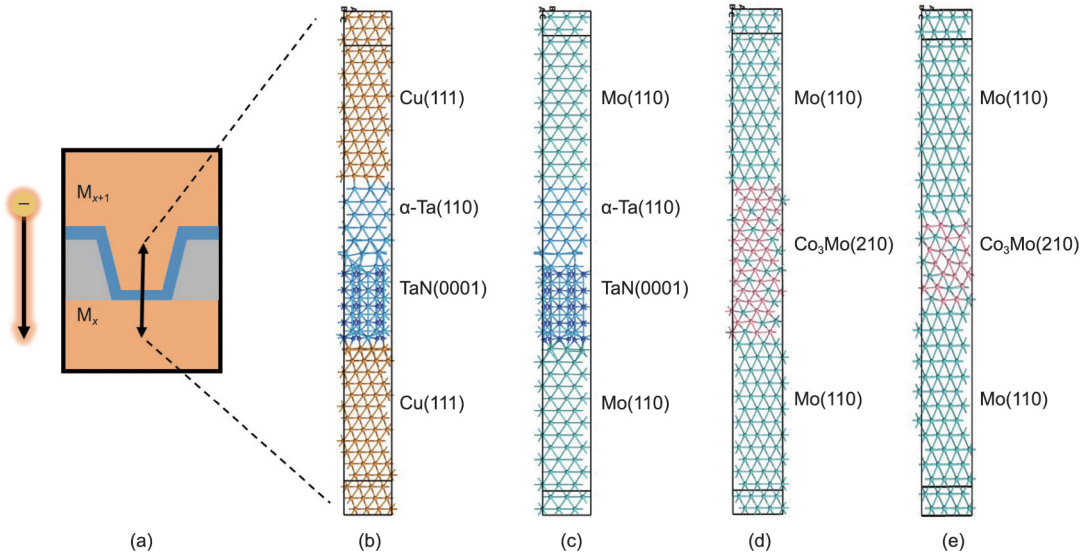

Fig. 7. Atomic structure participating in electron transport in the interconnect via structure. (a) Schematic of the interconnect via structure connecting the M_x and M_{x+1} layers. The electrons pass through the relatively high-resistance liner/barrier bilayer to the low-resistance layer. (b–e) Atomic-scale representation of the (b) Cu(111)/α-Ta(110)/TaN(0001)/Cu(111), (c) Mo(110)/α-Ta(110)/TaN(0001)/Mo(110), (d) Mo(110)/Co_3Mo(210) 3.0 nm/Mo(110), and (e) Mo(110)/Co_3Mo(210) 1.5 nm/Mo(110). Green spheres: Mo; pink spheres: Co; orange spheres: Cu; light blue spheres: Ta; dark blue spheres: N.

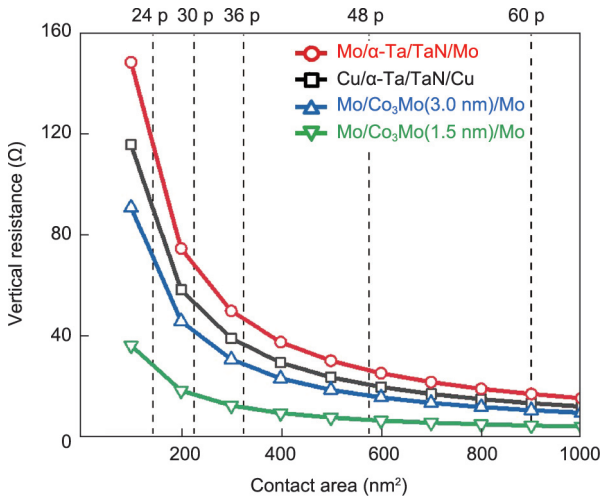

Fig. 8. Vertical resistance changes according to the contact area of each material constituting the via structure. The vertical dotted line indicates the contact area where the metal pitch occupies the same space, where 24 p means the 24 nm metal pitch and so on in a similar form.

To evaluate the effect on the vertical resistance in a real interconnect technology node, we divided the γ value in Table 2 by the effective cross-sectional area, plotted in Fig. 8. In the recently developed Intel 4 process node, the minimum metal pitch of the lowest layer is 30 nm. Assuming a symmetric line-to-line spacing, the interconnect width would be 15 nm, and the vertical interconnect would have an effective contact area of 225 nm^2. We indicated some representative BEOL pitches by means of dashed lines to understand the trend according to technology development. In a large cross-sectional area, the vertical resistance according to the structure does not show a significant difference. However, as the effective contact area decreases, the vertical resistance quickly approaches hundreds of ohms. When we replace the conventional structure with Mo-based materials, we can obtain a similar vertical resistance, even using a 24 nm metal pitch, where the 48 nm metal pitch area is reduced to a quarter. As scaling progresses, the interconnect structure composed of Mo-based materials will be more electrically competitive than the conventional Cu structure.

4. Conclusions

In this work, we developed strategies for synthesizing Mo-based nanowires using confined nanopores through Cu-damascene-process-friendly electrodeposition. We also characterized the effects of microstructure and phase differences on the electrical properties of the nanowires. We developed a method to inhibit the HER and electrodeposit metallic Mo onto confined nanopores. Adding boric acid to the acetate bath effectively suppressed the HER and allowed the synthesis of the largest crystalline Mo nanowire. TBA was most effective in inhibiting the HER but led to surface conduction that accelerated the reduction of the Mo precursor on the inner wall of the pores. However, it did not have a significant effect on resistivity. Mo nanowires with a diameter of 130 nm demonstrated a resistivity of (63.0 ± 17.9) μΩ·cm. Combining Co and Mo precursors with citrate ions allowed us to create Mo–Co nanowires whose resistivity was affected by changes in their composition and microstructure. Until the composition of the Co_3Mo intermetallic compound, the Mo_xCo_{1-x} ($0 < x < 0.28$ at%) alloy was electrically more suitable than the conventional barrier material, TaN. The DFT simulations showed that the Mo–Co intermetallic compound exhibits excellent adhesion to Mo, a potentially advanced interconnect material. Finally, the vertical resistance of a via of the Mo-based material calculated using DFT–NEGF showed a decrease of 21% compared with that of a conventional Cu interconnect structure. These findings suggest that advanced interconnect materials require appropriate barrier/liner materials and that Mo-based materials are appropriate materials for this task.

Acknowledgments

This work was supported by the Basic Science Research Program of the National Research Foundation of Korea, funded by the Ministry of Education of the Republic of Korea (2021R1A6A3A13046504), the Ministry of Science and ICT of the Republic of Korea (2022M3H4A1A04096339 and 2020M3F3A2A01081585), and the Samsung Electronics Co., Ltd. (IO210317-08500-01).

Compliance with ethics guidelines

Jun Hwan Moon, Taesoon Kim, Youngmin Lee, Seunghyun Kim, Yanghee Kim, Jae-Pyoung Ahn, Jungwoo Choi, Hyuck Mo Lee, and Young Keun Kim declare that they have no conflict of interest or financial conflicts to disclose.

Appendix A. Supplementary data

Supplementary data to this article can be found online at https://doi.org/10.1016/j.eng.2023.07.017.

References

[1] Gall D. The search for the most conductive metal for narrow interconnect lines. J Appl Phys 2020;127(5):050901.
[2] Witt C, Yeap KB, Leśniewska AA, Wan D, Jordan N, Ciofi I, et al. Testing the limits of TaN barrier scaling. In: Proceedings of the 2018 IEEE International Interconnect Technology Conference (IITC); 2018 Jun 4–7; Santa Clara, CA, USA. Piscataway: IEEE; 2018. p. 54–6.
[3] Lo CL, Helfrecht BA, He Y, Guzman DM, Onofrio N, Zhang S, et al. Opportunities and challenges of 2D materials in back-end-of-line interconnect scaling. J Appl Phys 2020;128(8):080903.
[4] Yeoh A, Madhavan A, Kybert N, Anand S, Shin J, Asoro M, et al. Interconnect stack using self-aligned quad and double patterning for 10nm high volume manufacturing. In: Proceedings of the 2018 IEEE International Interconnect Technology Conference (IITC); 2018 Jun 4–7; Santa Clara, CA, USA. Piscataway: IEEE; 2018. p. 144–7.
[5] Mont FW, Zhang X, Wang W, Kelly JJ, Standaert TE, Quon R, et al. Cobalt interconnect on same copper barrier process integration at the 7nm node. In: Proceedings of the 2017 IEEE International Interconnect Technology Conference (IITC); 2017 May 16–18; Hsinchu, China. Piscataway: IEEE; 2017. p. 1–3.
[6] Hegde G, Bowen RC, Simka H. A first-principles density functional theory based framework for barrier material screening. In: Proceedings of the 2018 IEEE International Interconnect Technology Conference (IITC); 2018 Jun 4–7; Santa Clara, CA, USA. Piscataway: IEEE; 2018. p. 163–5.
[7] Moon JH, Kim S, Kim T, Jeon YS, Kim Y, Ahn JP, et al. Electrical resistivity evolution in electrodeposited Ru and Ru–Co nanowires. J Mater Sci Technol 2022;105:17–25.
[8] Hsu KC, Perng DC, Yeh JB, Wang YC. Ultrathin Cr added Ru film as a seedless Cu diffusion barrier for advanced Cu interconnects. Appl Surf Sci 2012;258(18):7225–30.
[9] Hsu KC, Perng DC, Wang YC. Robust ultra-thin RuMo alloy film as a seedless Cu diffusion barrier. J Alloy Compd 2012;516:102–6.
[10] Kuo TC, Su YH, Lee WH, Liao WH, Wang YS, Hung CC, et al. A study on the plating and wetting ability of ruthenium–tungsten multi-layers for advanced Cu metallization. Microelectron Eng 2016;162:27–33.
[11] Yoo E, Moon JH, Jeon YS, Kim Y, Ahn JP, Kim YK. Electrical resistivity and microstructural evolution of electrodeposited Co and Co–W nanowires. Mater Charact 2020;166:110451.
[12] Hosseini M, Ando D, Sutou Y, Koike J. Co and $CoTi_x$ for contact plug and barrier layer in integrated circuits. Microelectron Eng 2018;189:78–84.
[13] Soulié JP, Tőkei Z, Swerts J, Adelmann C. Aluminide intermetallics for advanced interconnect metallization: thin film studies. In: Proceedings of the 2021 IEEE International Interconnect Technology Conference (IITC); 2021 Jul 6–9; Kyoto, Japan. Piscataway: IEEE, 2021. p. 1–3.
[14] Chen L, Chen Q, Ando D, Sutou Y, Kubo M, Koike J. Potential of low-resistivity Cu_2Mg for highly scaled interconnects and its challenges. Appl Surf Sci 2021;537:148035.
[15] Tang H, Tian Y, Wu Z, Zeng Y, Wang Y, Hou Y, et al. AC line filter electrochemical capacitors: materials, morphology, and configuration. Energy Environ Mater 2022;5(4):1060–83.

[16] Chen D, Zhao Z, Chen G, Li T, Chen J, Ye Z, et al. Metal selenides for energy storage and conversion: a comprehensive review. Coord Chem Rev 2023;479:214984.
[17] Zhao Z, Xia K, Hou Y, Zhang Q, Ye Z, Lu J. Designing flexible, smart and self-sustainable supercapacitors for portable/wearable electronics: from conductive polymers. Chem Soc Rev 2021;50(22):12702–43.
[18] Gall D. Electron mean free path in elemental metals. J Appl Phys 2016;119(8):085101.
[19] Tierno D, Hosseini M, van der Veen M, Dangol A, Croes K, Demuynck S, et al. Reliability of barrierless PVD Mo. In: Proceedings of the 2021 IEEE International Interconnect Technology Conference (IITC); 2021 Jul 6–9; Kyoto, Japan. Piscataway: IEEE, 2021. p. 1–3.
[20] Founta V, Soulié JP, Sankaran K, Vanstreels K, Opsomer K, Morin P, et al. Properties of ultrathin molybdenum films for interconnect applications. Materialia 2022;24:101511.
[21] Kresse G, Furthmüller J. Efficient iterative schemes for *ab initio* total-energy calculations using a plane-wave basis set. Phys Rev B 1996;54(16):11169–86.
[22] Kresse G, Furthmüller J. Efficiency of *ab-initio* total energy calculations for metals and semiconductors using a plane-wave basis set. Comput Mater Sci 1996;6(1):15–50.
[23] Perdew JP, Burke K, Ernzerhof M. Generalized gradient approximation made simple. Phys Rev Lett 1996;77(18):3865–8.
[24] Smidstrup S, Markussen T, Vancraeyveld P, Wellendorff J, Schneider J, Gunst T, et al. QuantumATK: an integrated platform of electronic and atomic-scale modelling tools. J Phys Condens Matter 2020;32(1):015901.
[25] Troullier N, Martins JL. Efficient pseudopotentials for plane-wave calculations. Phys Rev B Condens Matter 1991;43(3):1993–2006.
[26] Morley TJ, Penner L, Schaffer P, Ruth TJ, Bénard F, Asselin E. The deposition of smooth metallic molybdenum from aqueous electrolytes containing molybdate ions. Electrochem Commun 2012;15(1):78–80.
[27] Hasan SN, Xu M, Asselin E. Electrosynthesis of metallic molybdenum from water deficient solution containing molybdate ions and high concentrations of acetate. Surf Coat Tech 2019;357:567–74.
[28] Pachlhofer JM, Martín-Luengo AT, Franz R, Franzke E, Köstenbauer H, Winkler J, et al. Industrial-scale sputter deposition of molybdenum oxide thin films: microstructure evolution and properties. J Vac Sci Technol A 2017;35(2):021504.
[29] Oh MS, Yang BS, Lee JH, Oh SH, Lee US, Kim YJ, et al. Improvement of electrical and optical properties of molybdenum oxide thin films by ultralow pressure sputtering method. J Vac Sci Technol A 2012;30(3):031501.
[30] Munoz RC, Arenas C. Size effects and charge transport in metals: quantum theory of the resistivity of nanometric metallic structures arising from electron scattering by grain boundaries and by rough surfaces. Appl Phys Rev 2017;4(1):011102.
[31] Mayadas AF, Shatzkes M, Janak JF. Electrical resistivity model for polycrystalline films: the case of specular reflection at external surfaces. Appl Phys Lett 1969;14(11):345–7.
[32] Han JH, Khoo E, Bai P, Bazant MZ. Over-limiting current and control of dendritic growth by surface conduction in nanopores. Sci Rep 2014;4:7056.
[33] Zhang L, Kim SM, Cho S, Jang HJ, Liu L, Park S. Interfacial double layer mediated electrochemical growth of thin-walled platinum nanotubes. Nanotechnology 2017;28(3):035604.
[34] Jeon YS, Park BC, Ko MJ, Moon JH, Jeong E, Kim YK. Engineering the shape of one-dimensional metallic nanostructures via nanopore electrochemistry. Nano Today 2022;42:101348.
[35] Eliaz N, Gileadi E. Induced codeposition of alloys of tungsten, molybdenum and rhenium with transition metals. In: Vayenas CG, White RE, Gamboa-Aldeco ME, editors. Modern aspects of electrochemistry. New York City: Springer; 2008. p. 191–301.
[36] Gómez E, Pellicer E, Vallés E. Influence of the bath composition and the pH on the induced cobalt–molybdenum electrodeposition. J Electroanal Chem 2003;556:137–45.
[37] Rose RM, Shepard LA, Wulff J. The structure and properties of materials: electronic properties. 3rd ed. New York City: Wiley; 1967.
[38] Rossnagel SM. Characteristics of ultrathin Ta and TaN films. J Vac Sci Technol B 2002;20(6):2328–36.
[39] Seo Y, Lee S, Baek SC, Hwang WS, Yu HY, Lee SH, et al. The mechanism of Schottky barrier modulation of tantalum nitride/Ge contacts. IEEE Electron Device Lett 2015;36(10):997–1000.
[40] Guinier A. X-ray diffraction in crystals, imperfect crystals, and amorphous bodies. North Chelmsford: Courier Corporation; 1994.
[41] Dutta S, Sankaran K, Moors K, Pourtois G, Van Elshocht S, Bömmels J, et al. Thickness dependence of the resistivity of platinum-group metal thin films. J Appl Phys 2017;122(2):025107.
[42] Massalski TB, Okamoto H, Subramanian PR, Kacprzak L, editors. Binary alloy phase diagrams. ASM International: Materials Park; 1990.
[43] Gómez E, Pellicer E, Vallés E. Detection and characterization of molybdenum oxides formed during the initial stages of cobalt–molybdenum electrodeposition. J Appl Electrochem 2003;33(3/4):245–52.
[44] Beltowska-Lehman E, Indyka P. Kinetics of Ni–Mo electrodeposition from Ni-rich citrate baths. Thin Solid Films 2012;520(6):2046–51.
[45] Vanasupa L, Joo YC, Besser PR, Pramanick S. Texture analysis of damascene-fabricated Cu lines by X-ray diffraction and electron backscatter diffraction and its impact on electromigration performance. J Appl Phys 1999;85(5):2583–90.
[46] Gross ME, Drese R, Lingk C, Brown W, Evans-Lutterodt K, Barr D, et al. Electroplated damascene copper: process influences on recrystallization and texture. MRS Online Proc Library 1999;564:379.
[47] Philip TM, Lanzillo NA, Gunst T, Markussen T, Cobb J, Aboud S, et al. First-principles evaluation of fcc ruthenium for its use in advanced interconnects. Phys Rev Appl 2020;13(4):044045.
[48] Valencia D, Wilson E, Sarangapani P, Valencia-Zapata GA, Klimeck G, Povolotskyi M, et al. Grain boundary resistance in nanoscale copper interconnections. In: Proceedings of the 2016 International Conference on Simulation of Semiconductor Processes and Devices (SISPAD); 2016 Sep 6–8; Nuremberg, Germany. Piscataway: IEEE; 2016, p. 105–8.